Lattice Vibrations Change the Solid Solubility of an Alloy at High Temperatures

Nina Shulumba,[1,2] Olle Hellman,[3,1] Zamaan Raza,[1] Björn Alling,[1,4] Jenifer Barrirero,[2,1]
Frank Mücklich,[2] Igor A. Abrikosov,[1,5] and Magnus Odén[1]

[1]*Department of Physics, Chemistry, and Biology (IFM), Linköping University, SE-581 83 Linköping, Sweden*
[2]*Functional Materials, Saarland University, Campus D3 3, D-66123 Saarbrücken, Germany*
[3]*Division of Engineering and Applied Science, California Institute of Technology, Pasadena, California 91125, USA*
[4]*Max-Planck-Institut für Eisenforschung GmbH, D-40237 Düsseldorf, Germany*
[5]*Materials Modeling and Development Laboratory, NUST "MISIS," 119049 Moscow, Russia*
(Received 10 March 2015; revised manuscript received 7 August 2015; published 8 November 2016)

We develop a method to accurately and efficiently determine the vibrational free energy as a function of temperature and volume for substitutional alloys from first principles. Taking $Ti_{1-x}Al_xN$ alloy as a model system, we calculate the isostructural phase diagram by finding the global minimum of the free energy corresponding to the true equilibrium state of the system. We demonstrate that the vibrational contribution including anharmonicity and temperature dependence of the mixing enthalpy have a decisive impact on the calculated phase diagram of a $Ti_{1-x}Al_xN$ alloy, lowering the maximum temperature for the miscibility gap from 6560 to 2860 K. Our local chemical composition measurements on thermally aged $Ti_{0.5}Al_{0.5}N$ alloys agree with the calculated phase diagram.

When discussing the solubility of an alloy, the configurational entropy is always taken into account, but the effect of temperature associated with lattice vibrations is often neglected. It has been experimentally shown [1–4] that the vibrational and configurational entropies are comparable in the cases of fcc Ni_3Al and Cu_3Au and bcc Fe_3Al and FeCr, and theoretical studies draw the same conclusion [5–10] that lattice vibrations cannot be ignored. High-quality phonon spectra can be computed in the framework of density-functional perturbation theory [11] and the small displacement method [12], but the introduction of substitutional disorder as in an alloy causes the cost of such calculations to escalate rapidly. In this Letter, we propose a method of computing the vibrational free energy of a configurationally disordered solid based on the temperature-dependent effective potential method (TDEP) [13,14], which has an efficiency comparable to the state-of-the-art methods that only apply to ordered solids. Moreover, the method has the advantage of taking into account anharmonicity of the lattice vibrations and, therefore, remains valid at temperatures for which the quasiharmonic approximation breaks down.

We demonstrate the accuracy of our technique in a study of decomposition thermodynamics of $Ti_{1-x}Al_xN$ alloys [15,16], a system for which lattice vibrations underpin an unusual and technologically useful isostructural decomposition [17]. Metastable $Ti_{1-x}Al_xN$ coatings are ideal for use in the manufacturing of cutting tools due to their characteristic age hardening during use [18]. Metastable $Ti_{1-x}Al_xN$ with cubic $B1$ crystal structure undergoes spinodal decomposition to form nanoscale domains of $B1$ TiN- and AlN-rich phases, through which extra stress is required to propagate dislocations [16,19,20]. Remarkably, the calculated values of

the maximum temperature for the miscibility gap vary between approximately 7900 and 9000 K [21], depending on the methodological details, and as low as 3790 K [22] within the Debye-Grüneisen approximation. These are well above the dissociation temperatures of TiN and AlN, however, but cutting tools may reach temperatures of up to 1300 K [23], at which point vibrations could be of considerable importance and are subject to the effects of thermal expansion and anharmonicity. We note that existing studies either neglect or use an incomplete description of the vibrational contribution to the free energy, since the methodological challenge and computational efforts required to calculate the phonon spectra of a substitutionally disordered solid using *ab initio* approaches are considerable.

In this Letter, we propose a computationally tractable method for the treatment of vibrational free energy of a random alloy and use it to perform accurate first-principles calculations of the vibrational free energy of $B1$ $Ti_{1-x}Al_xN$ alloy, our model system. We derive a theoretical miscibility gap with a maximum temperature of 2860 K and show that the solubility limit of Al in TiN at intermediate temperatures is increased in comparison to calculations which neglect the effect of lattice vibrations. Our method employs the TDEP method to compute the vibrational contribution to the free energy. When constructing the phase diagram, we minimize the Gibbs free energy [24,25] to obtain the stable alloy compositions at equilibrium. We performed atom probe tomography experiments, exploiting the high spatial and chemical resolutions to depict the decomposition of a supersaturated solid solution of TiAlN with an alloy composition inside the miscibility gap, thus, verifying the predicted phase diagram and demonstrating the importance of lattice vibrations.

Our model system $Ti_{1-x}Al_xN$ alloy has the rocksalt structure, with the sites of the sodium sublattice occupied by N atoms, and Ti and Al atoms randomly distributed over the sites of the chlorine sublattice. Substitutional disorder of the Ti/Al sublattice is achieved using a special quasirandom structure (SQS) [26], although any other supercell approximation of the completely random alloy could be used. These atoms, however, interact with effective force constants which have full symmetry of the underlying crystal lattice. Lattice vibrations of the model system are described by the TDEP model Hamiltonian [13,14]:

$$\hat{H}_m = U_0 + \sum_i \frac{\mathbf{p}_i^2}{2m_i} + \frac{1}{2}\sum_{ij}\mathbf{u}_i\overset{=\text{eff}}{\Phi}_{ij}\mathbf{u}_j, \qquad (1)$$

where $\mathbf{p}_i$ and $\mathbf{u}_i$ are the momentum and displacement of atom i, $\overset{=\text{eff}}{\Phi}_{ij}$ are the second order effective force constant tensors, which relate the displacement of atom j to the force $\mathbf{f}_i$ exerted on atom i, and U_0 is a temperature-dependent reference energy. The TDEP method allows us to fit parameters of the model Hamiltonian to results of *ab initio* molecular dynamics simulations carried out for the real system of interest.

In the model Hamiltonian [Eq. (1)], the translational and spatial symmetry of the underlying crystal lattice are imposed by treating the components of the alloy as symmetry equivalent, and the real interactions present in density-functional theory (DFT) are mapped to effective interactions expressed by the interatomic effective alloy force constants $\overset{=\text{eff}}{\Phi}_{ij}$ corresponding to the underlying crystal lattice $B1$ in the case of $Ti_{1-x}Al_xN$. Imposing the symmetry reduces the number of independent components in $\overset{=\text{eff}}{\Phi}_{ij}$ considerably, making the method numerically efficient; thus, we call our approach the symmetry-imposed force constants TDEP method (SIFC TDEP). For example, in the $N = 128$ atom SQS, there are $3N \times 3N = 147456$ elements in the force constant matrix. If we consider interactions within the first five coordination shells and apply the symmetries as described, this number is reduced to 19 irreducible unknown components.

In our approach, the forces are obtained from calculations of the real disordered system as described by the SQS and only then mapped onto effective force constants in a system with randomly distributed atomic species having their respective correct atomic masses (i.e., there is only mass disorder in the TiAl sublattice). Note that the accuracy of the free energy calculations can always be improved, for example, by using a more complex model Hamiltonian. This can be achieved using an expansion of the pairwise force constants $AB, BC, AC\ldots$ resulting in different pairs for different pairs of species, although this is not necessary for our model system.

In order to find the effective force constant matrix that best represents the Born-Oppenheimer potential energy surface, we minimize the difference in forces between the model system and the SQS model of a real alloy, computing the latter by means of *ab initio* molecular dynamics (see the Supplemental Material [27]).

We calculate the internal energy via DFT [27] with the electronic contribution to the entropy given by the Mermin functional [35]. The configurational entropy is estimated using the mean-field approximation [36,37]. Short-range clustering effects in $Ti_{1-x}Al_xN$ have been shown to be significant and similar in magnitude to the mean-field contribution at temperatures below 3500 K [21]. In principle, such clustering effects should be included in the free energy calculations. However, in $Ti_{1-x}Al_xN$ they were found to predominantly impact the AlN-rich compositions, having little effect on the solubility limits in the TiN-rich region and only moderately decrease the maximum temperature of the miscibility gap. For these reasons, short-range clustering is not included in our calculations.

Phase stability at constant temperature and volume is determined by the Helmholtz free energy F. We decompose F into vibrational ("vib"), configurational ("config"), and electronic terms ("el"):

$$F = F_{\text{el}} + F_{\text{vib}} + F_{\text{config}}. \qquad (2)$$

Using the force constants in Eq. (1), we can calculate the phonon density of states $g(\omega, T)$ [38], from which we compute the vibrational contribution to the Helmholtz free energy:

$$F_{\text{vib}}(\omega, T) = \Delta U_0(T) + \int_0^\infty g(\omega, T)\frac{\hbar\omega}{2}d\omega$$
$$+ \int_0^\infty g(\omega, T)k_B T \ln\left(1 - \exp\left(-\frac{\hbar\omega}{k_B T}\right)\right)d\omega. \qquad (3)$$

In our case, $g(\omega, T)$ is strongly temperature dependent and includes anharmonic effects and thermal expansion. ΔU_0 is an anharmonic correction to the energy in TDEP formalism that is added to F_{vib} (see the Supplemental Material [27,38]).

The first test of our model system was to see that at low temperatures it does not deviate from a direct harmonic calculation using established methods [11,12], as illustrated in Fig. 1. The vibrational free energy of our model system agrees well with the harmonic model, with a difference of 2 meV/atom at 0 K and 4 meV/atom at 1500 K. For this to be a fair test, we used the TDEP force constants from 300 K where anharmonic contributions are expected to be negligible. This was a probe of the error introduced by the imposed symmetry, which turned out to be small.

At higher temperatures, the harmonic model is no longer a good benchmark, and we calculate the formally exact free energy difference using an implementation of TI [40,41]. Because of its considerable computational cost, it was applied to a single point, for which anharmonic effects are considerable. The discrepancy in the free energy at 1500 K
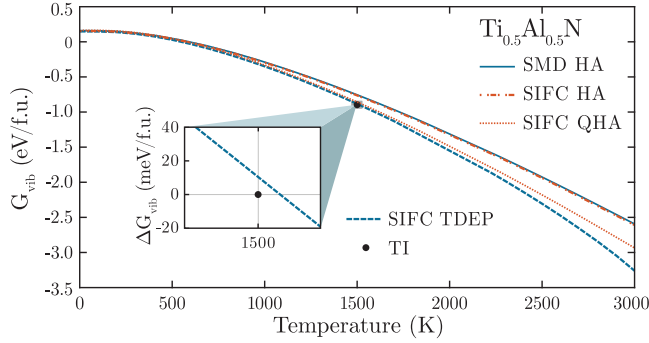
FIG. 1. Comparison of harmonic and anharmonic vibrational Gibbs free energies as a function of temperature, at zero pressure. Free energies were calculated in the harmonic approximation (HA) with symmetry-imposed force constants (SIFC) via the TDEP (SIFC HA) and small displacement (SMD HA) methods. Including thermal expansion as the only anharmonic effect results in the quasiharmonic approximation curve (SIFC QHA). The free energy including intrinsic anharmonic effects via the terms ΔU_0 and $g(\omega, T)$ from Eq. (3) (SIFC TDEP) is compared with a single thermodynamic integration data point (TI) as a benchmark. The differences between these methods are summarized in the Supplemental Material [27].

was calculated to be ~ 5 meV/atom. We note that the harmonic approximation is ~ 15 meV/atom further from the formally exact number (see Fig. 3 in the Supplemental Material [27,38]). We conclude that the SIFC TDEP and TI free energies are within our desired error bars, and we can use our model system free energies for the subsequent calculations with confidence.

We construct the Gibbs free energy ($G = F + PV$) from the Helmholtz free energy surface, where $P = -(\partial F/\partial V)|_T$. The Gibbs free energy of mixing is given by

$$G_{\mathrm{mix}}(T, x) = G_{\mathrm{Ti}_{1-x}\mathrm{Al}_x\mathrm{N}} - (1-x)G_{\mathrm{TiN}} - xG_{\mathrm{AlN}}, \quad (4)$$

where x is the fraction of AlN.

We reconstruct the concentration-temperature phase diagram at zero pressure by a direct minimization of G_{mix} at each temperature and global composition on a grid [42]. We determine the spinodal from the condition $((\partial^2 G_{\mathrm{mix}}/\partial x^2)|_T \leq 0)$. We note that at high temperatures and larger thermal expansions, some phonon frequencies may become imaginary in the quasiharmonic approximation due to the use of 0 K equilibrium configurations. TDEP does not suffer from this problem and facilitates the reconstruction of the entire phase diagram.

The calculated phase diagram is compared with one neglecting lattice vibrations in Fig. 2. The difference in both the spinodal region and the miscibility gap is dramatic. By including the vibrational contribution to the free energy, the maximum of the miscibility gap is lowered from 6560 to 2860 K. The roots of the second derivative of the total Gibbs free energy below 1000 K depend on the fitting function, in this case, third order Redlich-Kister polynomials [43] (gray lines of spinodal). In the quasiharmonic
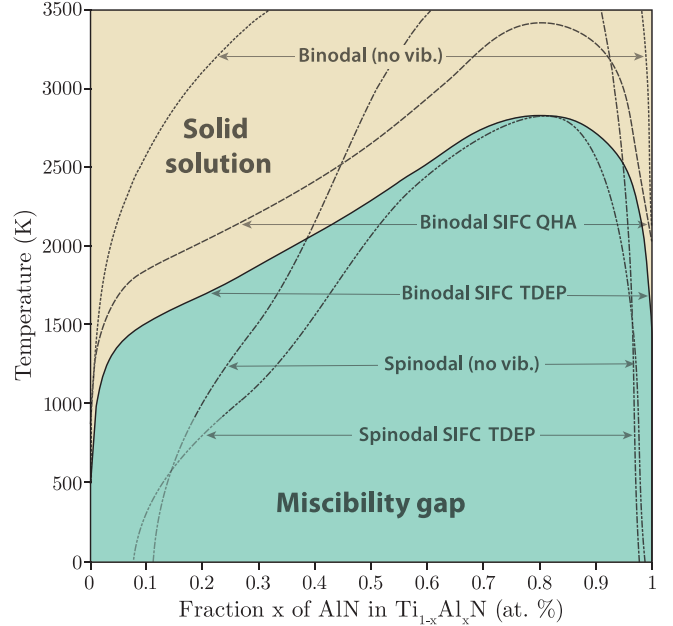

FIG. 2. Calculated phase diagram for $B1$-$\mathrm{Ti}_{1-x}\mathrm{Al}_x\mathrm{N}$. Comparing the dotted and solid lines shows the effect of including the anharmonic vibrational entropy for binodal using the SIFC TDEP method. The dash-dotted lines correspond to the spinodal metastable region including the anharmonic contribution and in the solid solution region to the spinodal line without the vibrational contribution. The binodal was also computed in the quasiharmonic approximation using the TDEP method (SIFC QHA) to demonstrate the effect of including thermal expansion but omitting temperature-induced intrinsic anharmonicity on the phase diagram.

approximation (QHA), thermal expansion effects are included but intrinsic anharmonicity is not; thus, the effects of intrinsic anharmonicity can be seen by comparing the QHA and TDEP boundaries in Fig. 2. Intrinsic anharmonicity has the effect of lowering the miscibility gap by approximately 500 K.

Experimental verification of the theoretical phase diagram (Fig. 2) is a challenging task. Because of the high melting temperature of TiN, its alloys are synthesized by thin-film deposition techniques, often followed by an annealing. Because of the explicit out-of-equilibrium nature of this metastable transformation, direct information from equilibrium experiments is not available, so we adopted the following strategy: 4 μm thick $\mathrm{Ti}_{1-x}\mathrm{Al}_x\mathrm{N}$ films with equal amounts of Ti and Al ($x = 0.5$) were deposited by cathodic arc evaporation, resulting in a nearly uniform solid solution [44]. Our theoretical predictions suggest that when diffusion is activated, this alloy will phase segregate through spinodal decomposition. To study this effect, a set of samples was prepared by annealing the $\mathrm{Ti}_{50}\mathrm{Al}_{50}\mathrm{N}$ films at 1073 K for 2, 4, 12, and 100 h in an argon atmosphere. The evolved microstructures were then examined by atom probe tomography.
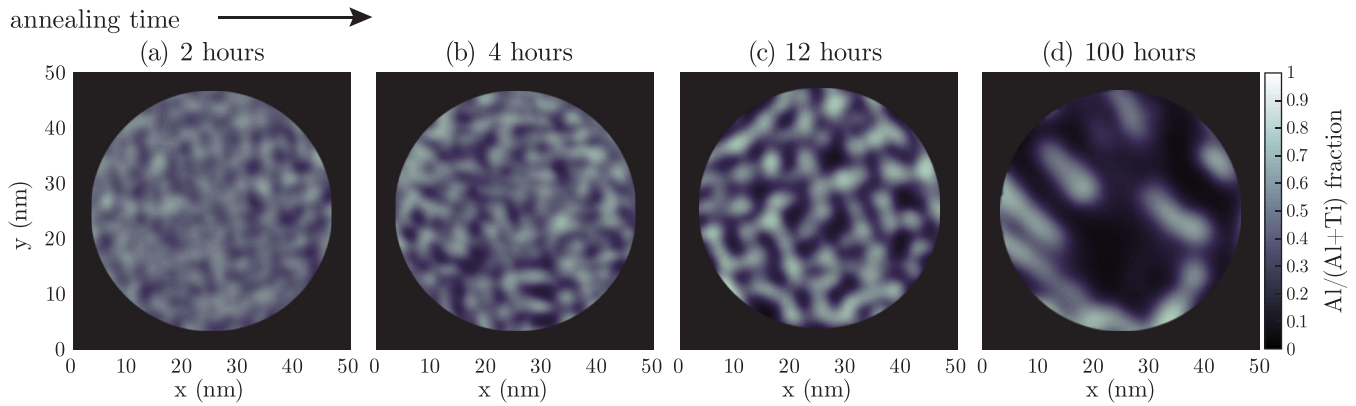
annealing time

FIG. 3.   Two-dimensional contour plots extracted from atom probe tomography data for different annealing times (a) 2 h, (b) 4 h, (c) 12 h and (d) 100 h.

Figure 3 shows 2D compositional maps of 2 nm thick slices through the reconstructed 3D atom probe specimen [45] of the annealed samples. The initially homogeneous cubic solid solution decomposes isostructurally forming cubic Ti- and Al-rich domains during the first 12 h. After 100 h, the metastable cubic AlN-rich phase has, to a large extent, transformed to its stable wurtzite phase [51]. During the first 12 h, the evolution of the microstructure and the chemical segregation becomes gradually more pronounced, which is consistent with the spinodal decomposition [52]. After 100 h, the microstructure is coarser.

The phase diagram (Fig. 2) shows a substantial shift in the solubility at 1073 K compared to the predictions excluding vibrational effects, especially for the solubility of Al in TiN. In order to experimentally verify this, we extracted the maximum and minimum local composition in the decomposed microstructure by constructing histograms of the concentrations in 1 nm^3 bins throughout the sample. These two local compositional extrema are plotted in Fig. 4 as a function of annealing time and demonstrate the time scale and decomposition path of the alloy. The solubility of Al in TiN at 1073 K tends to a final solubility of ∼2% according to the theoretical phase diagram. The solubility limit for Ti in cubic AlN could not be determined
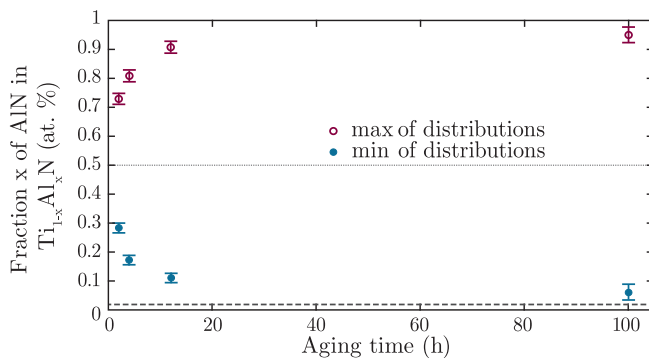
experimentally since it was not reached prior to the onset of wurtzite AlN formation. However, the experimental data for Ti in cubic AlN asymptotically approach the theoretical value ($x = 1$).

In summary, we present an accurate technique for calculating the vibrational contribution to the Gibbs free energy for random alloys. We reconstruct the phase diagram of a model $Ti_{1-x}Al_xN$ alloy and demonstrate that in this system, the nonharmonic vibrational phonon free energy is large and comparable to the harmonic energies. As a result, we find a dramatic decrease of the maximum temperature for the miscibility gap, from 6560 to 2860 K, as well as an increase AlN of solubility in TiN as compared to calculations which neglect lattice vibrations and anharmonicity. Atom probe tomography experiments on annealed $Ti_{0.5}Al_{0.5}N$ samples are in line with our theoretical predictions demonstrating a finite AlN content in the TiN-rich compositions after 100 h of annealing at 1073 K.

FIG. 4.   The limits of the concentration of metal sublattices as a function of aging time.

---

[1] L. Anthony, J. K. Okamoto, and B. Fultz, Phys. Rev. Lett. **70**, 1128 (1993).

[2] L. Anthony, L. J. Nagel, J. K. Okamoto, and B. Fultz, Phys. Rev. Lett. **73**, 3034 (1994).

[3] B. Fultz, L. Anthony, L. J. Nagel, R. M. Nicklow, and S. Spooner, Phys. Rev. B **52**, 3315 (1995).

[4] T. L. Swan-Wood, O. Delaire, and B. Fultz, Phys. Rev. B **72**, 024305 (2005).

[5] J. D. Althoff, D. Morgan, D. de Fontaine, M. Asta, S. M. Foiles, and D. D. Johnson, Phys. Rev. B **56**, R5705 (1997).

[6] A. van de Walle, G. Ceder, and U. V. Waghmare, Phys. Rev. Lett. **80**, 4911 (1998).

[7] V. Ozoliņš, C. Wolverton, and A. Zunger, Phys. Rev. B **58**, R5897 (1998).

[8] V. Ozoliņš and M. Asta, Phys. Rev. Lett. **86**, 448 (2001).

[9] A. van de Walle and G. Ceder, Rev. Mod. Phys. **74**, 11 (2002).

[10] B. Fultz, Prog. Mater. Sci. **55**, 247 (2010).

[11] S. Baroni, S. de Gironcoli, A. Dal Corso, and P. Giannozzi, Rev. Mod. Phys. **73**, 515 (2001).

[12] D. Alfè, Comput. Phys. Commun. **180**, 2622 (2009).

[13] O. Hellman, I. A. Abrikosov, and S. I. Simak, Phys. Rev. B **84**, 180301 (2011).

[14] O. Hellman, P. Steneteg, I. A. Abrikosov, and S. I. Simak, Phys. Rev. B **87**, 104111 (2013).

[15] A. Hörling, L. Hultman, M. Odén, J. Sjölén, and L. Karlsson, J. Vac. Sci. Technol. A **20**, 1815 (2002).

[16] P. H. Mayrhofer, A. Hörling, L. Karlsson, J. Sjölén, T. Larsson, C. Mitterer, and L. Hultman, Appl. Phys. Lett. **83**, 2049 (2003).

[17] A. Hörling, L. Hultman, M. Odén, J. Sjölén, and L. Karlsson, Surf. Coat. Technol. **191**, 384 (2005).

[18] G. Fox-Rabinovich, J. Endrino, B. Beake, A. Kovalev, S. Veldhuis, L. Ning, F. Fontaine, and A. Gray, Surf. Coat. Technol. **201**, 3524 (2006).

[19] R. Rachbauer, S. Massl, E. Stergar, D. Holec, D. Kiener, J. Keckes, J. Patscheider, M. Stiefel, H. Leitner, and P. H. Mayrhofer, J. Appl. Phys. **110**, 023515 (2011).

[20] M. Johansson Jõesaar, N. Norrby, J. Ullbrand, R. M'Saoubi, and M. Odén, Surf. Coat. Technol. **235**, 181 (2013).

[21] B. Alling, A. V. Ruban, A. Karimi, L. Hultman, and I. A. Abrikosov, Phys. Rev. B **83**, 104203 (2011).

[22] A. Wang, S.-L. Shang, Y. Du, L. Chen, J. Wang, and Z.-K. Liu, J. Mater. Sci. **47**, 7621 (2012).

[23] N. Norrby, L. Rogström, M. Johansson-Jõesaar, N. Schell, and M. Odén, Acta Mater. **73**, 205 (2014).

[24] J. W. Gibbs, *Transactions of the Connecticut Academy of Arts and Sciences*, Vol. 2 (Academy, New Haven, 1873), p. 382.

[25] J. W. Gibbs, *The collected works of J. Willard Gibbs* edited by W. R. Longley and R. G. Van Name, Vol. 1 (Longmans, Green, New York, 1928).

[26] A. Zunger, S.-H. Wei, L. G. Ferreira, and J. E. Bernard, Phys. Rev. Lett. **65**, 353 (1990).

[27] See Supplemental Material at http://link.aps.org/supplemental/10.1103/PhysRevLett.117.205502, which includes Refs. [28–34], for a description of TDEP method and free energy calculations. It includes computational details of the first principles calculations, thermodynamic integration, and a summary of acronyms and approximations used in the article.

[28] P. E. Blöchl, Phys. Rev. B **50**, 17953 (1994).

[29] G. Kresse and J. Hafner, Phys. Rev. B **48**, 13115 (1993).

[30] G. Kresse and J. Furthmüller, Phys. Rev. B **54**, 11169 (1996).

[31] G. Kresse and J. Furthmüller, Comput. Mater. Sci. **6**, 15 (1996).

[32] G. Kresse and D. Joubert, Phys. Rev. B **59**, 1758 (1999).

[33] S. Nosé, Mol. Phys. **52**, 255 (1984).

[34] H. J. Monkhorst and J. D. Pack, Phys. Rev. B **13**, 5188 (1976).

[35] N. D. Mermin, Phys. Rev. **137**, A1441 (1965).

[36] N. Saunders and A. P. Miodownik, *CALPHAD (Calculation of Phase Diagrams): A Comprehensive Guide* (Elsevier Science, New York, 1998.

[37] B. Fultz, *Phase Transitions in Materials* (Cambridge University Press, Cambridge, England, 2014).

[38] See Supplemental Material at http://link.aps.org/supplemental/10.1103/PhysRevLett.117.205502 for the phonon density of states calculations, which includes Ref. [39].

[39] G. Lehmann and M. Taut, Phys. Status Solidi B **54**, 469 (1972).

[40] D. Frenkel and B. Smit, *Computational Science Series* (Elsevier Science, New York, 2001).

[41] B. Grabowski, L. Ismer, T. Hickel, and J. Neugebauer, Phys. Rev. B **79**, 134106 (2009).

[42] C. Rossi, L. Cardozo-Filho, and R. Guirardello, Fluid Phase Equilib. **278**, 117 (2009).

[43] O. Redlich and A. T. Kister, Ind. Eng. Chem. Res. **40**, 341 (1948).

[44] L. Johnson, M. Thuvander, K. Stiller, M. Odén, and L. Hultman, Thin Solid Films **520**, 4362 (2012).

[45] See the Supplemental Material at http://link.aps.org/supplemental/10.1103/PhysRevLett.117.205502 for experimental details regarding atom probe tomography, which includes Refs. [46–50].

[46] K. Thompson, D. Lawrence, D. J. Larson, J. D. Olson, T. F. Kelly, and B. Gorman, Ultramicroscopy **107**, 131 (2007).

[47] D. N. Seidman, Annu. Rev. Mater. Res. **37**, 127 (2007).

[48] J. E. Allen, E. R. Hemesath, D. E. Perea, J. L. Lensch-Falk, Z. Li, F. Yin, M. H. Gass, P. Wang, A. L. Bleloch, R. E.

Palmer, and L. J. Lauhon, Nat. Nanotechnol. **3,** 168 (2008).

[49] Y.-J. Kim, J. D. Weiss, E. E. Hellstrom, D. C. Larbalestier, and D. N. Seidman, Appl. Phys. Lett. **105,** 162604 (2014).

[50] A. Biswas, D. J. Siegel, and D. N. Seidman, Acta Mater. **75,** 322 (2014).

[51] J. Endrino, C. Århammar, A. Gutiérrez, R. Gago, D. Horwat, L. Soriano, G. Fox-Rabinovich, D. Martín y Marero, J. Guo, J.-E. Rubensson, and J. Andersson, Acta Mater. **59,** 6287 (2011).

[52] A. Knutsson, J. Ullbrand, L. Rogström, N. Norrby, L. J. S. Johnson, L. Hultman, J. Almer, M. P. Johansson Jöesaar, B. Jansson, and M. Odén, J. Appl. Phys. **113,** 213518 (2013).